

PAPER

Pseudocapacitive Li-ion storage boosts high-capacity and long-life performance in multi-layer $\text{CoFe}_2\text{O}_4/\text{rGO}/\text{C}$ composite

To cite this article: Cong Wu *et al* 2019 *Nanotechnology* **30** 045401

View the [article online](#) for updates and enhancements.



IOP | ebooks™

Bringing you innovative digital publishing with leading voices to create your essential collection of books in STEM research.

Start exploring the collection - download the first chapter of every title for free.

Pseudocapacitive Li-ion storage boosts high-capacity and long-life performance in multi-layer $\text{CoFe}_2\text{O}_4/\text{rGO}/\text{C}$ composite

Cong Wu¹, Junyong Wang¹, Qinglin Deng¹, Mengjiao Li¹, Kai Jiang¹,
Liyan Shang¹, Zhigao Hu^{1,2}  and Junhao Chu¹

¹ Key Laboratory of Polar Materials and Devices (MOE) and Technical Center for Multifunctional Magneto-Optical Spectroscopy (Shanghai), Department of Electronic Engineering, East China Normal University, Shanghai 200241, People's Republic of China

² Collaborative Innovation Center of Extreme Optics, Shanxi University, Taiyuan, Shanxi 030006, People's Republic of China

E-mail: lyshang@ee.ecnu.edu.cn and zghu@ee.ecnu.edu.cn

Received 21 August 2018, revised 10 October 2018

Accepted for publication 1 November 2018

Published 22 November 2018



CrossMark

Abstract

Due to the intrinsic low electrical conductivity and large volume expansion of the CoFe_2O_4 based active materials, designing more novel structures is still one of the most important challenges for its lithium ion battery application. In this work, the CoFe_2O_4 /reduced graphene oxide/carbon (CFO/rGO/C) composite with integrated multi-layer structure has been synthesized through a facial two-step hydrothermal method. Benefiting from the introduction of the graphene network and amorphous carbon coating layer, as well as the accompanying synergistic effect, this composite can exhibit fast and reversible lithium intercalation/deintercalation reactions. With the aid of a surface-induced capacitive process, the CFO/rGO/C composite delivers a superior specific capacity (945 mA h g^{-1} at 0.1 A g^{-1}) and excellent long-term cyclic stability (421 mA h g^{-1} at 4 A g^{-1} with closely 100% Coulombic efficiency after 2000 cycles). Significantly, at a high current density of 1 A g^{-1} , the reversible capacity exhibits a rapid increasing after 100 cycles and finally shows an ultra-high-capacity of 1430 mA h g^{-1} over 500 cycles. This method could be generalized to the preparation of other similar transition metal oxide-based materials for the development of high-performance energy storage systems.

Supplementary material for this article is available [online](#)

Keywords: specific capacity, cyclic stability, Li-ion storage, $\text{CoFe}_2\text{O}_4/\text{rGO}/\text{C}$ composite

(Some figures may appear in colour only in the online journal)

1. Introduction

With ever-increasing energy consumption and the rapid development of various electrical vehicles, a great deal of effort has been devoted to widespread applications of multi-functional materials for the high-performance energy storage system [1–3]. Among these applications, rechargeable lithium ion batteries (LIBs) are given very high expectations as a promising energy storage conversion device due to stability, low cost, safety and being eco-friendly [4, 5]. However, the conventional commercial graphene materials have a low

theoretical lithium ion storage capacity of only 372 mA h g^{-1} , which can not fill the requirements of high power and high energy density for LIBs in real applications. In order to better improve the performance of LIBs, the preparation of more novel and advanced alternative materials, especially anode materials with higher energy density, larger rate capacity and longer cycle life span for the next-generation LIBs, is currently one of the most important challenges.

Recently, a large number of scientific researchers have focused their attention on the transition metal oxides (TMOs) including many binary TMOs (e.g. Fe_2O_3 , Co_3O_4 , MnO ,

TiO₂, etc) as well as ternary TMOs (e.g. CoFe₂O₄, ZnFe₂O₄, CoMn₂O₄, NiCo₂O₄, etc) with rationally structure design. They can deliver large theoretical capacity ranging from 500 to 1000 mA h g⁻¹, which is higher than that of graphene [6–12]. Compared with graphene, these TMOs based electrodes possess a unique lithium storage conversion mechanism. The transition metal cations are electrochemically reduced and embedded in the matrix of lithium oxide matrix. Meanwhile, the electrochemical redox potential is determined by the bonding state of the 3d orbital of the metal cation and the 2p orbital of the oxygen ion [13, 14]. Therefore, from a theoretical analysis, the lithium ion storage capacity of the TMOs is related to the oxidation state of their metal cations. Compared with the binary TMOs, the spinel bimetallic oxides with a common formula of AB₂O₄ (A, B = Mn, Fe, Co, Ni, Cu, Zn) possess two metallic elements leading to a higher oxidation state for a higher theoretical capacity. In the crystal structure, A²⁺ and B²⁺ metal cations occupy part or all of tetrahedral and octahedral positions, tightly surrounding the O²⁻ ion arrays. In the meantime, these compounds are not thermodynamic stable, which tend to generate abundant suitable vacancies and mixed metal valencies owing to the formation of antisite defects between A and B sites. This character could facilitate the insertion of lithium ions into the host material, providing a prominent electrochemical activity [15, 16]. Notably, according to the reaction mechanism (CoFe₂O₄ + 8Li⁺ + 8e⁻ → Co + 2Fe + 4Li₂O, 8 mol lithium per mol CoFe₂O₄ involve in the conversion process), CoFe₂O₄ delivers a high theoretic capacity of 916 mA h g⁻¹, which is two times higher than that of graphene [17–19]. What is more, in its crystal structure, the O 2p orbital energy level and Fe 3d orbital energy level are very close. It has a trend to form more Fe–O bondings with covalent bonding characteristics, which helps to enrich redox activity [20]. Moreover, CoFe₂O₄ also has some other merits, such as abundant reserves, low cost, eco-friendliness and ease of synthesis, which has shown great application prospects in the field of LIBs. Nevertheless, due to the intrinsic low conductivity and large volume expansion during the Li⁺ insertion and extraction process, the pure CoFe₂O₄ based electrode still faces the issues of rapid capacity degradation, terrible rate performance and poor cycle stability [17, 21, 22].

Among them, a common carbon-based material is graphene with some properties of large specific surface area, excellent electrical conductivity, superior mechanical strength. It can not only act as a stress buffer layer, relieve volume expansion, but also can be used as an excellent conductive matrix to enhance conductivity, making it an ideal candidate for excellent battery rate performance [23]. In our previous work, we have successfully combined it with different metal oxides and they all exhibited excellent electrochemical performance in LIBs [24–27]. However, there are different volume changes between the metal oxides and the graphene during the charge and discharge process, which easily lead to the peeling off of the metal oxide particles from the graphene framework and result in the capacity degradation after several cycles [28]. To effectively prevent the metal oxides nanoparticles separating from the graphene, it has been reported that

amorphous carbon layer can be used as a protective layer of the above composite. It can also serve as an additional conductive layer, which is beneficial to the cycle stability and rate characteristics of the active material [28–30].

In this work, taking the above two strategies into account, we have successfully synthesized an integrated multi-layer CoFe₂O₄/rGO/C hybrid through a facial two-step hydrothermal method with the introducing of graphene oxide and fructopyranose. During the hydrothermal reaction, graphene oxide (GO) was reduced into graphene flake and fructopyranose was pyrolyzed into amorphous carbon, serving as the structural framework and the protector, respectively. Compared with the pure CoFe₂O₄ or CoFe₂O₄/rGO electrode, this composite electrode delivers a large specific capacity (945 mA h g⁻¹ at 0.1 A g⁻¹, 734 mA h g⁻¹ at a high rate of 1 A g⁻¹) and excellent cycle stability (421 mA h g⁻¹ at 4 A g⁻¹ with the coulombic efficiency closely to 100% over 2000 cycles). Interestingly, it even delivers an ever-increasing capacity of 1430 mA h g⁻¹ after 500 cycles at a high current density of 1 A g⁻¹. We also discussed the storage mechanism of lithium ions from the internal battery structure and the pseudocapacitive mechanism in detail. Substantially, all these excellent electrochemical merits can benefit from this novel structure design.

2. Experimental section

2.1. Material preparation

Graphene oxide (GO) was synthesized by the oxidation of natural graphite nanoflakes according to a modified Hummer's method [31]. Typically, 60 mg GO was added to 15 ml deionized (DI) water, stirred for 24 h at room temperature and then intensively ultra-sonicated using an ultra-sonication probe (1000 W) for 30 min to form a uniform GO nanoflakes suspension A. 0.75 mmol Co(NO₃)₂ · 6H₂O, 1.5 mmol Fe(NO₃)₃ · 9H₂O were dissolved in 30 ml DI water and stirred uniformly for 30 min as solution B. The above A and B solution were homogeneous mixed, moderate amount of ammonia is added dropwise under magnetic stirring for another 30 min at room temperature to adjust the PH value of ~10. Finally, the mixture was transferred into a 50 ml Teflon-lined stainless steel autoclave and hydrothermally reaction at 200 °C for 10 h. After the autoclave cooled down to room temperature, the black jelly-like products were collected and washed with DI water and absolute ethyl alcohol several times respectively. Then the above products were redispersed in 20 ml DI water with adding 1 mmol fructopyranose and magnetic stirred for 30 min at ambient temperature. The solution was transferred into a 50 ml Teflon-lined stainless steel autoclave and hydrothermally reaction at 200 °C for 10 h again. The black products were centrifuged and washed with DI water three times. The final CoFe₂O₄/rGO/C nanocomposites were obtained by freeze-drying for 30 h. For comparison, pure CFO and rGO/CFO composite were also prepared by a similar process without GO or fructopyranose while keeping other conditions as constant.

2.2. Materials characterization

The crystal structures and crystallinity of the nanocomposites were characterized by x-ray diffraction (XRD, Bruker D8 Advance diffractometer) with Cu-K α radiation ($\lambda = 1.5418 \text{ \AA}$) from 10° to 80° . X-ray photoelectron spectroscopy (XPS) was performed on a RBD upgraded PHI-5000C ESCA system (PerkinElmer) with Mg-K α radiation ($h\nu = 1253.6 \text{ eV}$). Raman spectra were measured by a Jobin-Yvon LabRAM HR 800 micro-Raman spectrometer equipped with a 532 nm laser. Thermogravimetric analysis (TGA, TA Instruments 2000) was carried out over a temperature range from 30°C – 800°C in air with a heating rate of $10^\circ\text{C min}^{-1}$. The morphologies features and microstructures of nanocomposites were analyzed by field emission scanning electron microscopy (JEOL-JSM-6700F) equipped with energy dispersive x-ray spectroscopy (EDS). The transmission electron microscopy (TEM) images and selected area electron diffraction (SAED) of the samples were obtained by TEM (FEI Tecnai G2 F20) with an acceleration voltage of 200 KV.

2.3. Electrochemical measurement

The electrochemical properties of the nanocomposites were studied in CR2025 coin-type cells. The working electrodes were prepared by mixing as-fabricated samples, acetylene black, and polymer binder (polyvinylidene fluoride) with a mass ratio of 7:2:1 using N-methyl-2-pyrrolidinone as a solvent under magnetic stirring for 3 h at room temperature. Then the mixed slurry was uniformly pasted onto Cu foil as current collector and dried in a vacuum oven at 60°C overnight. The mass of loading active materials in each working electrode with a diameter of 12 mm was about 0.8 mg cm^{-2} . For the LIB test, the CR2025 half-cells with lithium foil as the counter electrode were assembled in an argon-filled glove box (Milkrona, Germany), where the concentrations of the oxygen and moisture below 1 ppm. The Celgard 2400 membrane and 1 mol L^{-1} LiPF $_6$ solution in a 1:1:1 (by volume) mixture of ethylene carbonate, dimethyl carbonate, ethyl methyl carbonate were used as the separator and the electrolyte respectively. Galvanostatic charge/discharge experiments were carried out in a LAND CT 2001A battery test system over a voltage window of 0.01–3.0 V (versus Li/Li $^+$). The cyclic voltammetry (CV) curves at a sweep rate of 0.1–10.0 mV s $^{-1}$ within a potential window of 0.01–3.0 V were performed on a CHI660 electrochemical workstation and the electrochemical impedance spectroscopy (EIS) were also tested in a CHI660 electrochemical workstation using an alternating current voltage with an amplitude of 5 mV in a frequency range of 0.01 Hz–100 kHz. All electrochemical experiments were conducted at room temperature.

3. Results and discussion

3.1. Structure and composition analysis

The preparation process and growth mechanism of the integrated multi-layer CFO/rGO/C composite is schematically

illustrated in figure 1(a). First and foremost, there are abundant hydrophilic oxygen-containing functional groups on the surface of GO. After a certain period of stirring and ultra-high power ultrasonic process, GO can become remarkable uniformly dispersed in the DI water and could be reduced to graphene over the entire hydrothermal process. Then, Co(NO $_3$) $_2 \cdot 6\text{H}_2\text{O}$ and Fe(NO $_3$) $_3 \cdot 9\text{H}_2\text{O}$ precursors were mixed sufficiently with GO solution. With the help of electrostatic attraction, hydrolyzed metal cations Co $^{2+}$, Fe $^{3+}$ in the solution can be absorbed in the oxygen-containing groups of the negatively charged graphene oxide flakes. During the heating process, the growing CFO nanoparticles were anchored on the surface of graphene, where the graphene flakes acted as the substrates and the functional groups served as the nucleation sites. With the further reaction progress, CFO nanoparticles were sufficiently embed in graphene flakes and can not be easily separated from the substrates. In return, G flakes with large area can prevent nanoparticles stacking together and provide a strong tendency for the composites to come into being a multi-layer structure, which can provide a large number of reaction sites favorable for energy storage. Subsequently, after a facial hydrothermal treatment again, fructopyranose was pyrolyzed into outer amorphous carbon film coated on the previous product resulting in the final integrated and stable multi-layer structure. Through this two-step hydrothermal reaction, outside amorphous carbon coating layer and inner graphene formed a multi-layer conductive framework, which can reduce the diffusion resistance of the ions and electrons and alleviate volume expansion during the charge/discharge process.

In figure 1(b), the crystalline structure and phase information of the as-prepared samples were analyzed. The XRD characteristic diffraction peaks located at 18.3° , 30.0° , 35.4° , 43.1° , 53.4° , 57.0° , 62.6° , 74.0° can be indexed to the (111), (220), (311), (400), (422), (511), (440), (533) crystal faces of face-centered cubic spinel CoFe $_2$ O $_4$ structure (space group: Fd3m, JCPDS card no. 22-1086) [17, 19]. As can be seen, all three XRD patterns are consistent and there are no other extra peaks corresponding to carbon or other impurities, indicating the fine crystallinity. In other words, amorphous coating carbon has little effect on the the crystallinity of the as-synthesized products.

The Raman spectra of CFO/rGO and CFO/rGO/C nanocomposites are shown in figure 1(c). A series of vibration peaks appear in low-wavenumber region (100 – 1000 cm^{-1}) corresponding to A $_{1g}$, E $_g$ and 3T $_{2g}$ of CoFe $_2$ O $_4$ crystal [32]. In addition, Raman spectra exhibits two main peaks, disordered (D) and graphite (G) bands, where the D band (1350 cm^{-1}) comes from a breathing mode of *k*-point phonon of A $_{1g}$ symmetry and the G band (1590 cm^{-1}) arises from the first-order scattering of the E $_{2g}$ phonon of carbon atom. In figure S1, available online at stacks.iop.org/NANO/30/045401/mmedia, the CFO/rGO and CFO/rGO/C nanocomposites display the increased intensity ratio of the D and G band (D/G) compared with GO, indicating that the degree of disorder increases and graphene is reduced. It can be ascribed to the restoration of numerous graphitic in-plan sp 2 domains and the increased number of

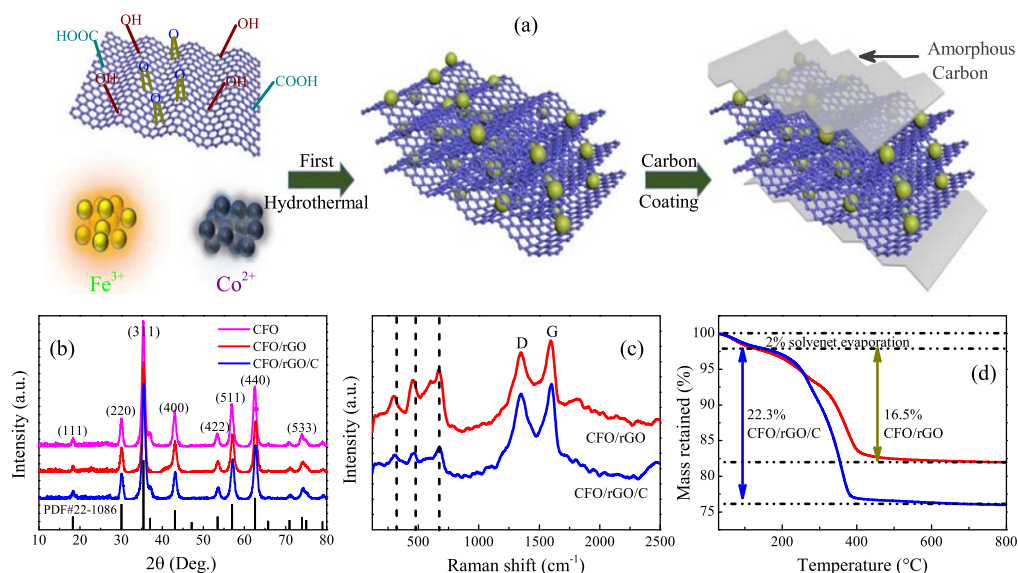


Figure 1. (a) Schematic illustration of the synthesis procedure for CFO/rGO/C nanocomposites with multi-layer structure; (b) XRD patterns of as-prepared nanocomposite; (c) Raman spectra of CFO/rGO, and CFO/rGO/C composites; (d) TGA of CFO/rGO, CFO/rGO/C composites.

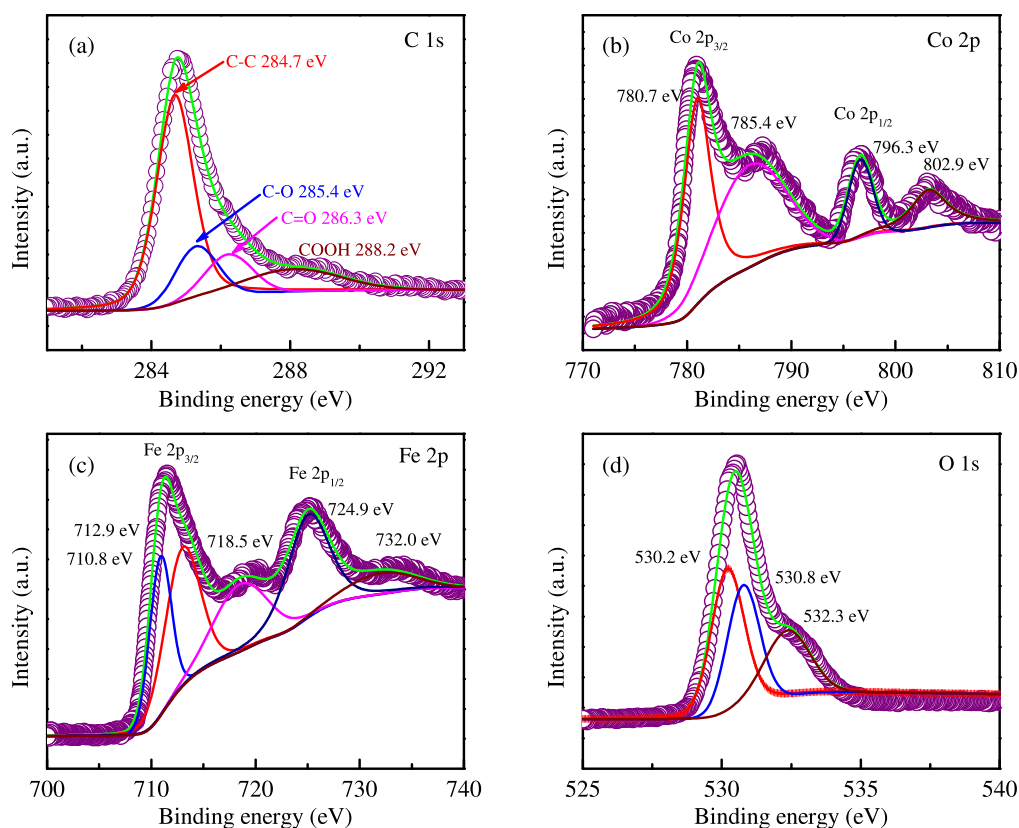


Figure 2. High-resolution XPS for the CFO/rGO/C nanocomposite: (a) C 1s, (b) Co 2p, (c) Fe 2p and (d) O 1s, respectively.

the domains [33, 34]. As shown in figure 1(d), the weight percentage of CoFe_2O_4 nanoparticles, graphene and amorphous carbon were estimated based on TGA analysis of CFO/rGO and CFO/rGO/C compounds. At about 100°C , because of the evaporation of residual solvent, a small amount of weight loss of 2% is emerging. When the

temperature reaches above 420°C , graphene and amorphous carbon were completely oxidized and decomposed, resulting in 16.5% and 22.3% weight loss in CFO/rGO and CFO/rGO/C compounds, respectively. It further certifies the present of amorphous carbon coating layer of 5.8 wt% after the second hydrothermal.

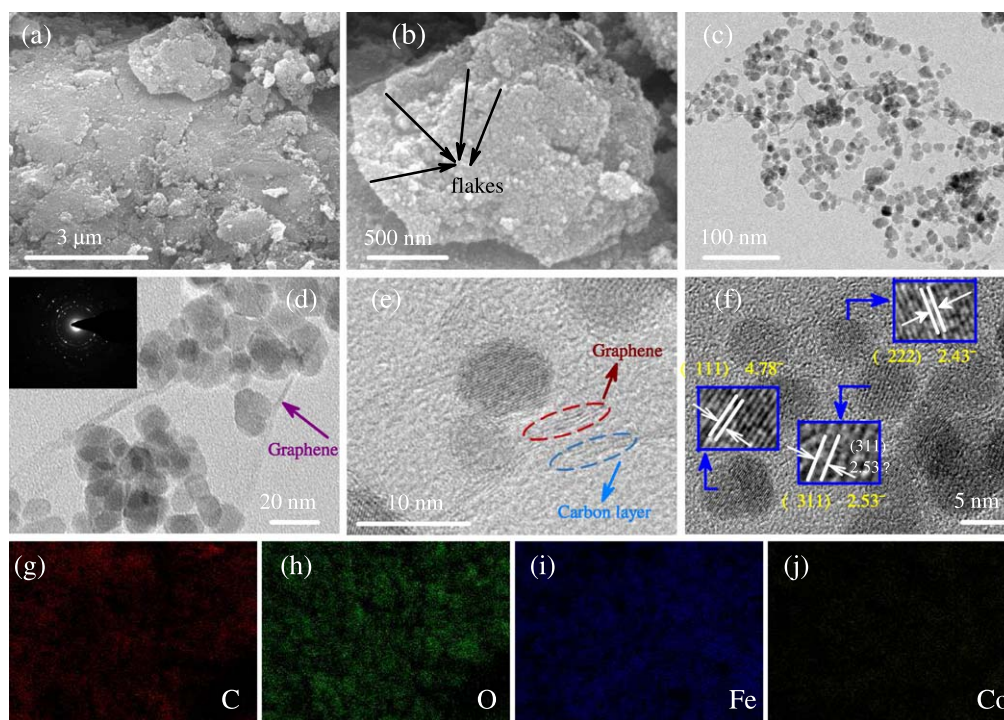


Figure 3. (a) SEM and (b) high magnification SEM images of the CFO/rGO/C nanocomposite. The black arrows indicate the multi-layer structure composite. (c)–(f) TEM, high magnification TEM, high-resolution TEM images and high-resolution TEM images of the CFO/rGO/C nanocomposite. The inset image of (d) shows the SAED pattern. (g)–(j) The corresponding elemental mapping images of C, O, Fe and Co for the CFO/rGO/C nanocomposite.

To investigate the valence state and surface chemical composition, XPS was conducted. Figure 2 displays the entire XPS spectrum containing all the characteristic peaks, which reveals the presence of C 1s, Co 2p, Fe 2p and O 1s without any other impurity element. The high-resolution C 1s spectrum (figure 2(a)) exhibits four peaks at 284.7 eV, 285.4 eV, 286.3 eV and 288.2 eV, corresponding to non-oxygenated C, C–O, C=O, HO–C=O, respectively [35]. The dominating non-oxygenated C reflects the good conductivity for CFO/rGO/C. In the Co 2p spectrum (figure 2(b)), the first two dominating peaks with binding energy of about 780.7 eV and 785.4 eV corresponding to Co 2p^{3/2} and its shakeup satellite peak. Obviously, we could see that the strong satellite peaks locate at around 4.7 eV above the binding energy of the Co 2p^{3/2} peaks, indicating that there are a good deal of divalent Co ions in the as-synthesized products [17]. The de-convoluted Fe 2p spectra (figure 2(c)), the first fitting peaks (located at 710.8 eV and 712.9 eV) for Fe 2p^{3/2} are consistent with the tetrahedral and octahedral sites, respectively. However, the other higher peaks with the binding energy of about 724.9, 718.5 and 732.0 eV belong to Fe 2p^{1/2} and its shakeup satellite peaks, revealing that the iron element is 3+ in the sample [36]. In addition, the high-resolution O 1s spectra (figure 2(d)) can be fitted into three peaks at 530.2 eV, 530.8 eV and 532.3 eV, which can be assigned to the lattice oxygen in (Co/Fe)-oxygen framework, surface absorbed hydroxyl oxygen or carbonate species, and C–O or O=C–O functional groups in graphene, respectively [37, 38]. As a result, the entire XPS spectrum demonstrates the formation of cobalt ferrite nanoparticles.

3.2. Surface morphologies

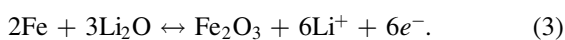
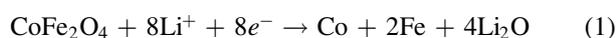
The as-synthesized CFO, CFO/rGO, CFO/rGO/C have been characterized by SEM and TEM to further evaluate the morphology and microstructure shown in figures 3(a)–(f) and figure S3. Obviously, all the samples present a dense appearance and the nanoparticles are closely packed. Particularly, with the participation of GO, the hybrids exhibit an integrated interconnected structure with CFO nanoparticles, which are uniformly decorated on graphene flakes. The high magnification SEM image of CFO/rGO/C composite (figure 3(b)) clearly reveals that the G flakes and those ultrafine CFO nanoparticles combine to form sheets. They were alternately arranged and formed a multi-layer structure, which is evidenced from the folded edges. On the one hand, with the help of confining effect of graphene flakes, the CFO nanoparticles are homogeneously distributed in the carbon frameworks instead of stacking together. On the other hand, CFO nanoparticles can act as separator, which effectively separate graphene and prevent agglomeration due to its hydrophobic nature. Consequently, the formed conductive network can facilitate the transport of lithium ions and electrons during the charge–discharge process.

Figures 3(c) and S4 show the TEM image of CFO/rGO/C and CFO/rGO nanocomposites and further confirm that the CFO nanoparticles are well dispersed on the graphene substrate before and after the carbon coating process. The CFO nanoparticles have a size of about 10 nm in the magnified TEM image (figure 3(d)). In figure 3(e), the wrinkled fringes at the edge indicate a graphene conductive matrix and

a outer amorphous carbon layer, respectively, which can facilitate the transport of Li ions. Moreover the graphene marked by the arrow in figure 3(d) is thin and transparent, indicating a single graphene layer of CFO/rGO/C. Compared with it, the graphene layer is darker and less transparent than that of CFO/rGO as noted in figure S4. It suggests that the successful wrapping of amorphous carbon is attached to the outer layer of the composite and it is consistent with the results from the previous TGA test. The high-resolution TEM image (figure 3(f)) exhibits the lattice fringes of 2.43 Å, 2.53 Å and 4.87 Å corresponding to the (222), (311) and (111), respectively and further reflects the good crystallinity of the CFO nanocrystalline. Impressively, the EDS elemental mapping (figures 3(g)–(i)) further reveals the well distribution of C, O, Fe and Co through the entire composite, confirming that the CFO nanoparticles are homogeneously dispersed on the graphene network from another point of view.

3.3. Energy storage applications

In order to study the effect of the introduction of the graphene and amorphous carbon on the electrochemical performance, the CFO, CFO/rGO and multi-layer CFO/rGO/C were evaluated as electrode materials for lithium batteries. Figures 4(a)–(c) display the similar CV of these three electrodes for the initial five cycles at a scan rate of 0.5 mV s⁻¹ in the potential window from 0.01 to 3.0 V versus Li/Li⁺, indicating the similar electrochemical reactions. Consistent with the previous reports, CFO, CFO/rGO and CFO/rGO/C electrodes distinctly exhibit the dominating peaks at 0.51 V, 0.53 V and 0.52 V in the first cathodic scan, which can be attributed to the reduction of Fe³⁺ and Co²⁺ to metallic Fe⁰ and Co⁰ along with the formation of the amorphous solid Li₂O, as well as the irreversible reaction with the electrolyte and come into being a solid electrolyte interface (SEI) film [18, 21, 22]. As compared with the first cycle, the cathodic peak intensity minish and shift to the high potential in the following cycles, implying the irreversible phase transformation in the first cycle and can result in a capacity decay during this electrochemical process [39]. Meanwhile, the weak and broad anodic peaks located at 1.80, 1.72 and 1.65 V (for CFO, CFO/rGO and CFO/rGO/C) are corresponding to the oxidation of metallic iron and cobalt to Fe³⁺ and Co²⁺ in the first anodic scan [22, 40], which shift to high voltage about 1.93V, 1.87 V and 1.9 V in the second and following cycles resulting from the polarization of electrode materials. It is worth noting that the subsequent CV profiles tend to stable and almost overlap, implying the good electrochemical reversibility and cyclic stability for the CFO/rGO/C electrode. Moreover, the entire electrochemical process can be expressed as follows: [17–19, 41]



To better shed light on the electrochemical kinetics of the CFO based electrodes, we analyzed the stepwise lithium mechanism by measuring the CV curves of CFO, CFO/rGO and CFO/rGO/C electrodes at various scan rates. In figures 4(d)–(f), it is clear that the shape of the CFO based electrodes redox peaks almost have no change when the scan rate is varried from 0.1 to 1.0 mV s⁻¹. Furthermore, compared with CFO and CFO/rGO, the peak voltage offsets of CFO/rGO/C with the increase of sweep rate are very tiny, suggesting the fast lithium intercalation and deintercalation kinetics of the electrode with the small polarization. Along with the lithiation process, the effects of diffusion-controlled intercalation process (DIP) and surface-induced capacitive process (SCP) can be distinguished from the power-law relationship: $i = a\nu^b$ [42–44], where the i and ν represent the measured current and the scan rate, respectively. Note that, the value of b can be obtained from the slope of the $\log(\nu)$ – $\log(i)$ plot and a , b values are approaching. In particular, for the DIP part, b equals to 0.5 and the i is proportional to the square root of the ν and controlled by the semi-infinite linear diffusion. For the SCP part, b equals to 1 and the i is related to the ν . As shown in figure 4(i), the $\log(V)$ – $\log(i)$ plots of CFO/rGO/C electrode are well presented. The values of b are fitted to be about 0.78 and 0.87 for the anodic and cathodic peak when the scan rate ranges from 0.1 to 1.0 mV s⁻¹. Obviously, these b values are higher than bare CFO (figure 4(g)) or CFO/rGO (figure 4(h)) electrodes. It indicates that they can provide the flexible electron and ion transport path, enhance the surface conductivity after the introducing of graphene network and amorphous carbon coating layer. Therefore, the CFO/rGO/C electrodes exhibit the surface-induced capacitive dominated mechanism and the fast reaction kinetics. In the light of the general relationship: $i = k_1\nu + k_2\nu^{1/2}$ [45, 46], the percentage of capacitive contribution of surface capacitance effects can be quantitatively obtained through calculating the coefficient fraction of k_1 and k_2 at every potential voltage. In the red region of figure S6, higher than 87.8% of the total capacity was verified as the capacitive contribution for the CFO/rGO/C electrode at 1.0 mV s⁻¹, which was higher than 87.2% of CFO/rGO sample and 46.4% of CFO sample. And these qualified results matched well with the the slope feature of the $\log(V)$ – $\log(i)$ plots (figures 5(g)–(i)), the higher value of b , the better reaction kinetics of in the multi-layer 3D architecture electrode. It can realize faster charge transfer and led to improved electrochemical performance. It can also be seen that there is a change in the slope at lager sweep rate rang from 3 to 10 mV s⁻¹ (figure S5). When the rate >3 mV s⁻¹, the slopes decrease to 0.64 and 0.57 for the anodic and cathodic peaks, respectively. As previously described, when the DIP dominated, the values of b will approach to 0.5, which result in the limitation to the rate capability. This is probable because that there is an increase in the ohmic contribution originating from SEI resistance, active material resistance, or diffusion limitation [47, 48].

The galvanostatic charge–discharge curves of the CFO/rGO/C electrode for the 1st, 2nd, 5th, and 30th cycles with the current density of 100 mA g⁻¹ over the voltage window

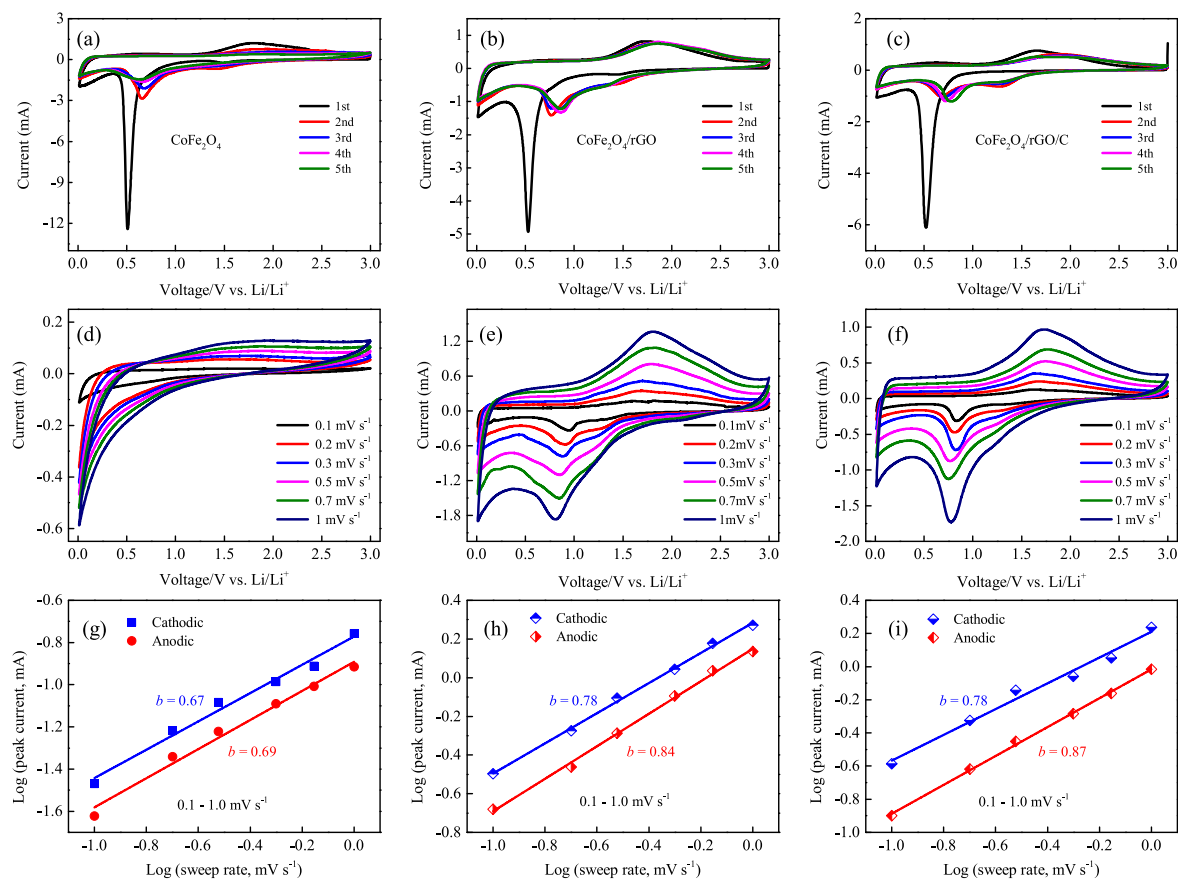


Figure 4. The pseudocapacitance mechanism analysis of lithium storage behavior (a)–(c) CV curves of the CFO, CFO/rGO and CFO/rGO/C electrodes at a scan rate of 0.5 mV s^{-1} in the window of $0.01\text{--}3.0 \text{ V}$ versus Li/Li^+ . (d)–(f) CV curves at different scan rates for the CFO, CFO/rGO and CFO/rGO/C electrode. (g)–(i) Relationship between logarithm peak current and logarithm scan rates for the CFO, CFO/rGO and CFO/rGO/C electrodes, respectively.

between 0.01 and 3 V are presented in figure 5(a). In the first discharge process (i.e. the lithium ion insertion process), the CFO/rGO/C hybrids demonstrate a long potential plateau at about 0.78 V during the lithium ion insertion process. It can be seen that there is also an observable discharge plot ranging from 0.87 to 0.01 V . This may be relevant to the insertion of lithium ion into carbon composed of graphene and amorphous coating carbon [17], which reflects the capacity contribution of the carbon materials. The theoretical capacity value of CFO/rGO/C electrode can be calculated as follow: $\text{Capacity}_{\text{theoretical}} = \text{Capacity}_{\text{carbon}} \times \text{wt\% (carbon)} + \text{Capacity}_{\text{CoFe}_2\text{O}_4} \times \text{wt\% (CoFe}_2\text{O}_4) = 372 \text{ mA h g}^{-1} \times 22.3 \text{ wt\%} + 916 \text{ mA h g}^{-1} \times 77.7 \text{ wt\%} = 795 \text{ mA h g}^{-1}$. Obviously, the CFO/rGO/C electrode exhibits the initial discharge and charge capacity of 1465 mA h g^{-1} and 979 mA h g^{-1} , much higher than the theoretical capacity. It may be ascribed to the synergistic effect of the CFO and carbon-based materials (graphene and coating carbon). Nevertheless, the initial coulombic efficiency is only 67% and the initial irreversible capacity loss can be attributed to the partial conversion of Fe_2O_3 and CoO_2 and the partial deposition of electrolyte. The formation of a SEI film could also result in the irreversible lithium ion loss [18, 21, 39]. However, in the second cycle, the discharge and charge capacity are 960 and 950 mA h g^{-1} , respectively, with a higher coulombic efficiency of 99% . Meanwhile, after the first cycle, the

discharge and charge profiles are almost overlapped without the significant change for the 2nd, 5th and 30th cycles, demonstrating the good cyclic stability and reversibility.

To better evaluate the rate performance of the CFO based electrodes, the cells were tested at various current density ranging from 0.1 A g^{-1} to 4 A g^{-1} , as shown in figure 5(c). The CFO/rGO/C composite displays the average discharge capacity of $945, 892, 826, 734, 610$ and 484 mA h g^{-1} at the current density of $0.1, 0.2, 0.5, 1, 2$ and 4 A g^{-1} , respectively, with the corresponding charge and discharge profiles in figure 5(b). Particularly, when the current density is restored to 0.1 A g^{-1} , the average discharge capacity can be recovered to as high as 963 mA h g^{-1} quickly, implying excellent rate performance for fast lithiation/delithiation. Obviously, the CFO/rGO/C electrode exhibits the superior rate performance and good stability than other controlled electrodes at the high current density stage. Especially, for the bare CFO electrode, without the graphene and coating carbon, the discharge capacity significantly declines from initial 912 mA h g^{-1} to ultimate 10 mA h g^{-1} with increasing current density. Even when the current goes back to 0.1 A g^{-1} , it can only return to 143 mA h g^{-1} , which is much lower than the CFO/rGO/C hybrid. When the CFO/rGO/C electrode was tested in a short-term cycling process at a small current density of 0.1 A g^{-1} (figure 6(a)), it exhibited an ever-increasing capacitance. It is

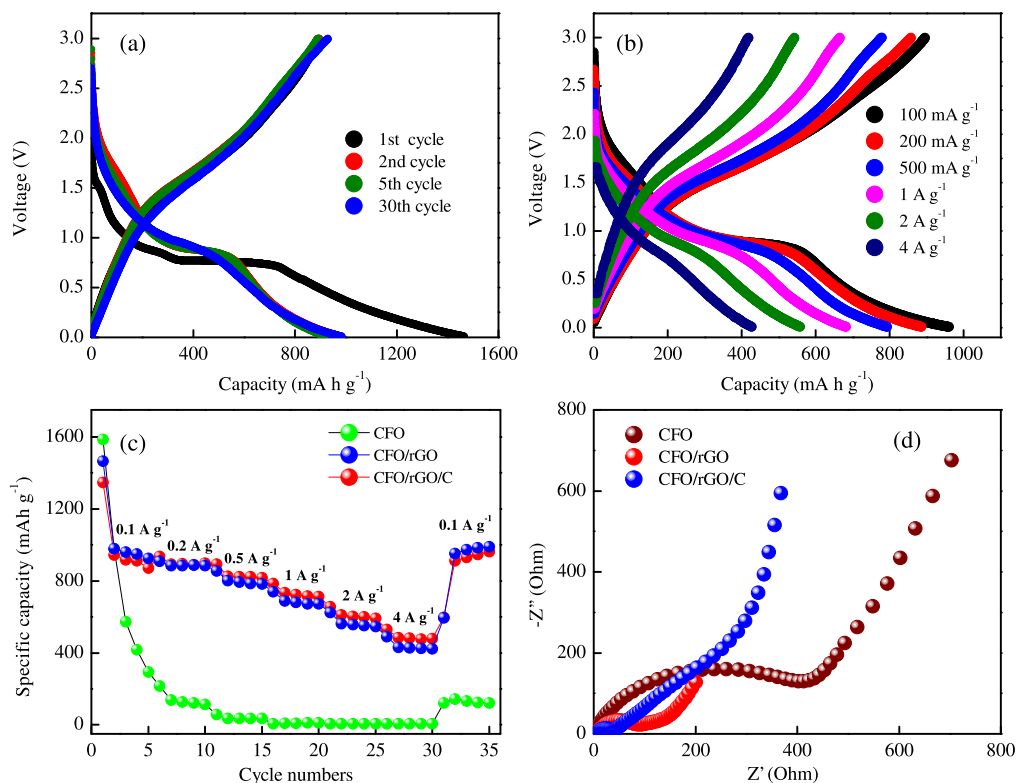


Figure 5. (a) Galvanostatic charge–discharge curves for 1st, 2nd, 5th and 30th cycle of the CFO/rGO/C electrode at 0.1 A g^{-1} . (b) Charge and discharge voltage profiles of the CFO/rGO/C electrode and (c) the rate performance of the CFO based electrode at different current density varying from 0.1 A g^{-1} to 4 A g^{-1} . (d) The electrochemical impedance spectra (EIS) for the active materials.

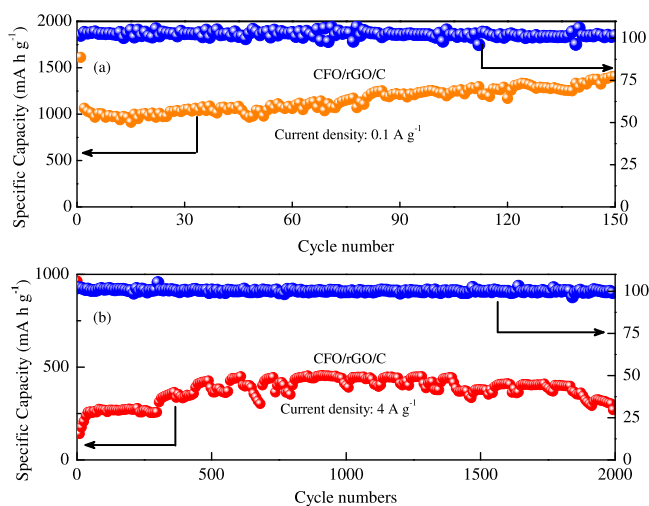


Figure 6. (a) Short-term and (b) long-term cycling performance and coulombic efficiency of CFO/rGO/C at 0.1 A g^{-1} and 4 A g^{-1} , respectively.

worth noting that, even at the high current density of 4 A g^{-1} , the long-term cycling performance of CFO/rGO/C electrode displays a substantially steady profile (figure 6(b)) with an average high reversible capacity of 421 mA h g^{-1} with almost 100% coulombic efficiency over 2000 cycles, reflecting the outstanding durability for this hybrid. Therefore, such superior electrochemical performance of CFO/rGO/C can be attributed to the cleverly structural design with multi-layer graphene and

coating carbon. On one hand, the multi-layer graphene as the conductive matrix contributes to the transport of lithium ion and electron because of its extraordinary conductive properties. On the other hand, the outer carbon coating film can further enhance the conductivity of the material and act as a protective layer to avoid some unfavorable side reactions between CFO and the organic electrolyte in the charge–discharge process. Furthermore, the integrated multi-layer framework can not only efficiently provide the volume change buffer space, but also inhibit the self-agglomeration of CFO particles during the cycling process. To further demonstrate remarkable rate performance and good cyclability of the CFO/rGO/C hybrid, the EIS measurements were performed. In figure 5(d), it is obvious that all these three EIS have similar semicircles in the high/medium frequency regions, corresponding to the contact resistance and charge transfer resistance, as well as sloping lines due to the mass transport of lithium ions in the low frequency region. Notably, the CFO/rGO/C electrode shows the smallest semicircle and the steepest sloping line in the impedance spectrum, manifesting the lowest charge transfer resistance and fast lithium ion diffusion kinetics profited by the multi-layer graphene and carbon coating layer. All these features are in good agreement with the above mentioned improved rate performance for novel CFO/rGO/C electrode.

To better demonstrate the advantages of the cyclic performance properties of the CFO/rGO/C hybrid for LIBs, the long-term cycling profiles at a rate of 1 A g^{-1} are presented in figure 7(a). Evidently, in this long-term cycle, the specific

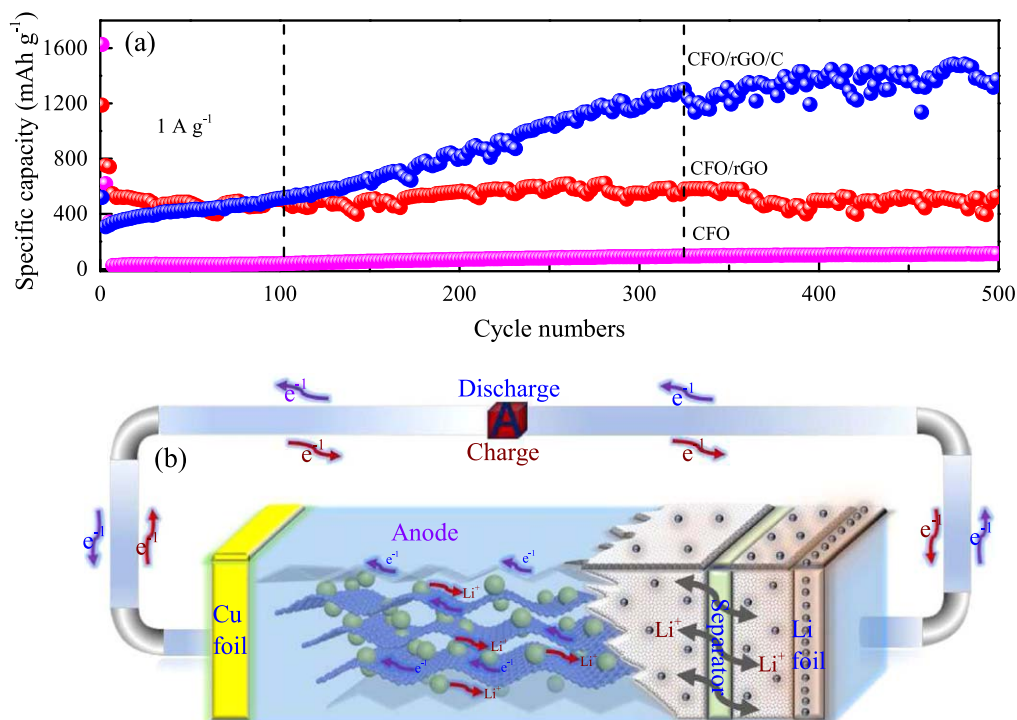


Figure 7. (a) Cycling performance at a rate of 1 A g⁻¹ for the as-synthesized cells; (b) schematic illustration of the internal half-cell structure and improved ion charge transfer mechanism.

capacity of CFO/rGO/C is higher than that of other samples overall. More interestingly, the entire cycle profile of CFO/rGO/C seem to be divided into three stages, which goes through stabilization, transient increasing and durability process, respectively. In the early stage, due to the formation of SEI film on the surface of the electrode and partial deposition of electrolyte, the cell is incompletely activated and exhibits the average specific capacity of only $\sim 435 \text{ mA h g}^{-1}$ in the first 100 laps. With the gradual penetration of electrolyte, deeper activation of internal materials, the storage of lithium has been significantly improved. Finally, it adapts to the rapid volume change caused by the insertion and extraction of lithium ions, and the structure tends to be stable. The hybrid possesses a capacity up to 1430 mA h g^{-1} after 500 cycles, which is much higher than previous reported capacity of CFO based materials. Such a charming electrochemical phenomenon deservedly benefits from the rational structural design.

Figure 7(b) describes the whole half-cell structure and the transport kinetics of electron and lithium ion during the entire charge–discharge process in detail. Firstly, graphite has the loose porous structure characteristics that can help the rapid penetration of the electrolyte. It could facilitate the CFO nanoparticles to sufficiently contact with the electrolyte, minimize the lithium ion transmission path during the lithium ion intercalation and deintercalation process. At the same time, graphene can in turn act as a conductive matrix, accelerating the flexible transport of electron. Meanwhile, the multi-layer graphene framework can effectively inhibit self-agglomeration of CFO particles in the reaction. It could also well limits the volume expansion of the internal structure and the pulverization of the electrode, guaranteeing satisfactory

rate and cycle properties. Furthermore, the outer layer of amorphous carbon coating acts as a protector of the internal electrode, suppressing some of the adverse reactions. On the other hand, the layer is also a kind of conductive element, and further contribute to the fast charge transfer. Moreover, the integrated hybrid structure can generate the synergistic effects among CFO nanoparticles, graphene and carbon layer, forming a surface-induced capacitive dominated mechanism. It realizes the fast reaction kinetics and eventually producing a steadily strengthened pseudocapacitance much higher than the theoretical capacity value of CFO or graphene.

4. Conclusion

In summary, we have demonstrated a novel strategy to synthesis an integrated $\text{CoFe}_2\text{O}_4/\text{rGO}/\text{C}$ hybrid with multi-layer structure through a facial two-step hydrothermal method. The graphene acts as a structural framework, fructopyranose becomes the outer carbon coating layer and the CoFe_2O_4 nanoparticles are well confined in this 3D conductive framework. Benefited from this novel structural design, the CFO/rGO/C electrode delivers a large specific capacity of 945 mA h g^{-1} at 0.1 A g^{-1} , 734 mA h g^{-1} at a high rate of 1 A g^{-1} and a stable cycle capacity of 421 mA h g^{-1} at a high rate of 4 A g^{-1} over 2000 cycles. In particular, the reversible capacity exhibits a rapidly increasing phenomena and eventually up to 1430 mA h g^{-1} at 1 A g^{-1} in a 500-lap cycle, much higher than the other CFO based materials. All these outstanding electrochemical properties can be ascribed to the introduction of graphene and

amorphous carbon coating layer, which mitigate the volume expansion of the electrode, shorten the ion transport path and enhance charge transfer. Moreover, the synergistic effect of the CFO nanoparticles, graphene and carbon coating layer could realize the strengthened pseudocapacitive storage. Therefore, we believe that the novel structure design, mechanism analysis, and excellent electrochemical properties could bring references to related TMO-based materials as well as promote the development and application for high-performance energy storage devices.

Acknowledgments

This work was financially supported by the National Key R&D Program of China (Grant Nos. 2017YFA0303403 and 2018YFB0406500), the National Natural Science Foundation of China (Grant Nos. 61674057 and 61227902), the Projects of Science and Technology Commission of Shanghai Municipality (Grant Nos. 18JC1412400, 18YF1407200, and 18YF1407000), and the Program for Professor of Special Appointment (Eastern Scholar) at Shanghai Institutions of Higher Learning and the Fundamental Research Funds for the Central Universities.

ORCID iDs

Zhigao Hu  <https://orcid.org/0000-0003-0575-2191>

References

- [1] Kundu D, Talaie E, Duffort V and Nazar L F 2015 The emerging chemistry of sodium ion batteries for electrochemical energy storage *Angew. Chem., Int. Ed. Engl.* **54** 3431–48
- [2] Choi S H, Ko Y N, Lee J K and Kang Y C 2015 3D MoS₂-graphene microspheres consisting of multiple nanospheres with superior sodium ion storage properties *Adv. Funct. Mater.* **25** 1780–8
- [3] Goodenough J B and Park K S 2013 The Li-ion rechargeable battery: a perspective *J. Am. Chem. Soc.* **135** 1167–76
- [4] Dunn B, Kamath H and Tarascon J M 2011 Electrical energy storage for the grid: a battery of choices *Science* **334** 928–35
- [5] Wang N, Bai Z C, Qian Y T and Yang J 2016 Double-walled Sb@TiO_{2-x} nanotubes as a superior high-rate and ultralong lifespan anode material for Na-ion and Li-ion batteries *Adv. Mater.* **28** 4126–33
- [6] Jiang T C, Bu F X, Feng X X, Shakir I, Hao G L and Xu Y X 2017 Porous Fe₂O₃ nanoframeworks encapsulated within three-dimensional graphene as high-performance flexible anode for lithium-ion battery *ACS Nano* **11** 5140–7
- [7] Chu Y T et al 2018 Embedding MnO@Mn₃O₄ nanoparticles in an N-doped-carbon framework derived from Mn-organic clusters for efficient lithium storage *Adv. Mater.* **30** 1704244
- [8] Yang J P et al 2017 Amorphous TiO₂ shells: a vital elastic buffering layer on silicon nanoparticles for high-performance and safe lithium storage *Adv. Mater.* **29** 1700523
- [9] Dong Y C, Zhang Z Y, Xia Y, Chui Y S, Lee J M and Zapfen J A 2015 Green and facile synthesis of Fe₃O₄ and graphene nanocomposites with enhanced rate capability and cycling stability for lithium ion batteries *J. Mater. Chem. A* **3** 16206–12
- [10] Jiang B B, Han C P, Li B, He Y J and Lin Z Q 2016 In-situ crafting of ZnFe₂O₄ nanoparticles impregnated within continuous carbon network as advanced anode materials *ACS Nano* **10** 2728–35
- [11] Li J F, Xiong S L, Li X W and Qian Y T 2013 A facile route to synthesize multiporous MnCo₂O₄ and CoMn₂O₄ spinel quasi-hollow spheres with improved lithium storage properties *Nanoscale* **5** 2045–54
- [12] Wang Y, Liu P C, Zhu K J, Wang J and Liu J S 2017 Hierarchical bilayered hybrid nanostructural arrays of NiCo₂O₄ micro-urchins and nanowires as a free-standing electrode with high loading for high-performance lithium-ion batteries *Nanoscale* **9** 14979–89
- [13] Xi K, Chen B G, Li H L, Xie R S, Gao C L, Zhang C, Kumar R V and Robertson J 2015 Soluble polysulphide sorption using carbon nanotube forest for enhancing cycle performance in a lithium-sulphur battery *Nano Energy* **12** 538–46
- [14] Xi K, Kidambi P R, Chen R, Gao C, Peng X, Ducati C, Hofmann S and Kumar R V 2014 Binder free three-dimensional sulphur/few-layer graphene foam cathode with enhanced high-rate capability for rechargeable lithium sulphur batteries *Nanoscale* **6** 5746–53
- [15] Ma F X, Yu L, Xu C Y and Lou X W 2016 Self-supported formation of hierarchical NiCo₂O₄ tetragonal microtubes with enhanced electrochemical properties *Energy Environ. Sci.* **9** 862–6
- [16] Yu H J, Ren Y, Xiao D D, Guo S H, Zhu Y B, Qian Y M, Gu L and Zhou H S 2014 An ultrastable anode for long-life room-temperature sodium-ion batteries *Angew. Chem., Int. Ed. Engl.* **53** 8963–9
- [17] Xia H, Zhu D D, Fu Y S and Wang X 2012 CoFe₂O₄-graphene nanocomposite as a high-capacity anode material for lithium-ion batteries *Electrochim. Acta* **83** 166–74
- [18] Li Z H, Zhao T P, Zhan X Y, Gao D S, Xiao Q Z and Lei G T 2010 High capacity three-dimensional ordered macroporous CoFeO as anode material for lithium ion batteries *Electrochim. Acta* **55** 4594–8
- [19] Xiong Q Q, Tu J P, Shi S J, Liu X Y, Wang X L and Gu C D 2014 Ascorbic acid-assisted synthesis of cobalt ferrite (CoFe₂O₄) hierarchical flower-like microspheres with enhanced lithium storage properties *J. Power Sources* **256** 153–9
- [20] Grimaud A, Hong W T, Shao-Horn Y and Tarascon J M 2016 Anionic redox processes for electrochemical devices *Nat. Mater.* **15** 121–6
- [21] Dong B T, Li M Y, Xiao C H, Ding D W, Gao G X and Ding S J 2017 Tunable growth of perpendicular cobalt ferrite nanosheets on reduced graphene oxide for energy storage *Nanotechnology* **28** 055401
- [22] Ren S H, Zhao X Y, Chen R Y and Fichtner M 2014 A facile synthesis of encapsulated CoFe₂O₄ into carbon nanofibres and its application as conversion anodes for lithium ion batteries *J. Power Sources* **260** 205–10
- [23] Zhang B, Zheng Q B, Huang Z D, Oh S W and Kim J K 2011 SnO-graphene-carbon nanotube mixture for anode material with improved rate capacities *Carbon* **49** 4524–34
- [24] Wang J Y, Deng Q L, Li M J, Wu C, Jiang K, Hu Z G and Chu J H 2018 Facile fabrication of 3D porous MnO@GS/CNT architecture as advanced anode materials for high-performance lithium-ion battery *Nanotechnology* **31** 315403
- [25] Deng Q L, Li M J, Wang J Y, Jiang K, Hu Z G and Chu J H 2018 Free-anchored Nb₂O₅@graphene networks for ultrafast-stable lithium storage *Nanotechnology* **29** 185401
- [26] Wang J Y, Deng Q L, Li M J, Jiang K, Hu Z G and Chu J H 2018 High-capacity and long-life lithium storage boosted by

- pseudocapacitance in three dimensional MnO-Cu-CNT/graphene anodes *Nanoscale* **10** 2944–54
- [27] Li M J, Deng Q L, Wang J Y, Jiang K, Hu Z G and Chu J H 2018 *In-situ* carbon encapsulation of vertical MoS₂ arrays with SnO₂ for durable high rate lithium storage: dominant pseudocapacitive behavior *Nanoscale* **10** 741–51
- [28] Zhang C F, Peng X, Guo Z P, Cai C B, Chen Z X, Wexler D, Li S and Liu H K 2012 Carbon-coated SnO₂/graphene nanosheets as highly reversible anode materials for lithium ion batteries *Carbon* **50** 1897–903
- [29] Li D, Seng K H, Shi D Q, Chen Z X, Liu H K and Guo Z P 2013 A unique sandwich-structured C/Ge/graphene nanocomposite as an anode material for high power lithium ion batteries *J. Mater. Chem. A* **1** 14115–21
- [30] Wang D N, Yang J L, Li X F, Geng D S, Li R Y, Cai M, Tsun-Kong S and Sun X L 2013 Layer by layer assembly of sandwiched graphene/SnO₂ nanorod/carbon nanostructures with ultrahigh lithium ion storage properties *Energy Environ. Sci.* **6** 2099–906
- [31] Hummers W S and Offerman R E 1958 Preparation of graphitic oxide *J. Am. Chem. Soc.* **80** 1339
- [32] Sousa M H, Tourinho F A and Rubim J C 2000 Use of Raman micro-spectroscopy in the characterization of MIIFe₂O₄ (M = Fe, Zn) electric double layer ferrofluids *J. Raman Spectrosc.* **31** 185–91
- [33] Ferrari A C and Robertson J 2000 Interpretation of Raman spectra of disordered and amorphous carbon *Phys. Rev. B* **61** 14095
- [34] Petnikota S, Teo K W, Chen L, Sim A, Marka S K, Reddy M V, Srikanth V V, Adams S and Chowdari B V 2016 Exfoliated graphene oxide/MoO₂ composites as anode materials in Li ion batteries: an insight into intercalation of Li and conversion mechanism of MoO₂ *ACS Appl. Mater. Interfaces* **6** 10884
- [35] Liu D H, Lu H Y, Wu X L, Hou B H, Wan F, Bao S D, Yan Q Y, Xie H M and Wang R S 2015 Constructing the optimal conductive network in MnO-based nanohybrids as high-rate and long-life anode materials for lithium-ion batteries *J. Mater. Chem. A* **3** 19738–46
- [36] Reddy M V, Sharma N, Adams S, Rao R P, Peterson V K and Chowdari B V R 2015 Evaluation of undoped and M-doped TiO₂, where M = Sn, Fe, Ni/Nb, Zr, V, and Mn, for lithium-ion battery applications prepared by the molten-salt method *RSC Adv.* **5** 29535–44
- [37] Yuan W Y, Yuan J, Xie J L and Li C M 2016 Polymer-mediated self-assembly of TiO₂@Cu₂O core-shell nanowire array for highly efficient photoelectrochemical water oxidation *ACS Appl. Mater. Interfaces* **8** 6082–92
- [38] Reddy M V, Xu Y M, Rajarajan V, Ouyang T Y and Chowdari B V R 2015 Template free facile molten synthesis and energy storage studies on MCo₂O₄ (M = Mg, Mn) as anode for Li-ion batteries *ACS Sustain. Chem. Eng.* **3** 3035–42
- [39] Li S M, Wang B, Liu J H and Yu M 2014 In situ one-step synthesis of CoFe₂O₄/graphene nanocomposites as high-performance anode for lithium-ion batteries *Electrochim. Acta* **129** 33–9
- [40] Zhang Z L, Wang Y H, Zhang M J, Tan Q Q, Lv X, Zhong Z Y and Su F B 2013 Mesoporous CoFe₂O₄ nanospheres cross-linked by carbon nanotubes as high-performance anodes for lithium-ion batteries *J. Mater. Chem. A* **1** 7444–50
- [41] Zhao S H, Guo J X, Jiang F, Su Q M and Du G H 2016 Porous CoFe₂O₄ nanowire arrays on carbon cloth as binder-free anodes for flexible lithium-ion batteries *Mater. Res. Bull.* **79** 22–8
- [42] Chao D L et al 2016 Array of nanosheets render ultrafast and high-capacity Na-ion storage by tunable pseudocapacitance *Nat. Commun.* **7** 12122
- [43] Li S, Qiu J X, Lai C, Ling M, Zhao H J and Zhang S Q 2015 Surface capacitive contributions: towards high rate anode materials for sodium ion batteries *Nano Energy* **12** 224–30
- [44] Wang H Y, Jiang H, Hua Y J, Saha P, Cheng Q L and Li C Z 2017 Interface-engineered MoS₂/C nanosheet heterostructure arrays for ultra-stable sodium-ion batteries *Chem. Eng. Sci.* **174** 104–11
- [45] Chao D L et al 2018 A high-rate and stable quasi-solid-state zinc-ion battery with novel 2D layered zinc orthovanadate array *Adv. Mater.* **30** 1803181
- [46] Chao D L et al 2016 Pseudocapacitive Na-Ion storage boosts high rate and areal capacity of self-branched 2D layered metal chalcogenide nanoarrays *ACS Nano* **10** 10211–9
- [47] Chen C J, Wen Y W, Hu X L, Ji X L, Yan M Y, Mai L Q, Hu P, Shan B and Huang Y H 2015 Na⁺ intercalation pseudocapacitance in graphene-coupled titanium oxide enabling ultra-fast sodium storage and long-term cycling *Nat. Commun.* **6** 6929
- [48] Augustyn V, Come J, Lowe M A, Kim J W, Taberna P L, Tolbert S H, Abruna H D, Simon P and Dunn B 2013 High-rate electrochemical energy storage through Li⁺ intercalation pseudocapacitance *Nat. Mater.* **12** 518–22